NATIONAL INSTITUTE FOR FUSION SCIENCE

Nonlinear Simulation of Resistive Ballooning Modes in Large Helical Device

H. Miura, T. Hayashi and T. Sato

RESEARCH REPORT
NIFS Series

TOKI, JAPAN

Nonlinear simulation of resistive ballooning modes in Large Helical Device

Hideaki MIURA, Takaya HAYASHI and Tetsuya SATO,

Theory and Computer Simulation Center,

National Institute for Fusion Science,

Oroshi 322-6.Toki.Gifu 509-5292, JAPAN

Abstract

Nonlinear simulations of a magneto-hydrodynamic (MHD) plasma in full three-dimensional geometry of the Large Helical Device (LHD) are conducted to study nonlinear evolution of pressure-driven instabilities. A series of simulations for a resistive plasma shows growth of resistive ballooning instability. The growth rate of the most unstable resistive ballooning mode is shown to be proportional to the one-third power of the resistivity. Nonlinear saturation of the instability and its slow decay are observed. After the nonlinear saturation, the pressure takes a profile similar to so-called *pedestal*. A possible scenario of nonlinear relaxation of a plasma toward a new equilibrated state is discussed.

KEYWORD: nonlinear simulation. MHD. resistive ballooning mode

I. INTRODUCTION

The LHD system [1] is a heliotron/ torsatron type helical device with a plane magnetic axis with two helical coils. where the pitch period number $M = 10$ and the aspect ratio of the major radius to the average minor radius of a plasma is 6.5. A series of experimental programs by using the LHD are now under way and some successful results have been reported. [2,3] Since macro-scale plasma fluctuations in the LHD system are considered to be dominated by pressure-driven instabilities, understanding linear and nonlinear behaviors of this kind of instability is important to achieve good confinement. Pressure-driven instabilities are important not only for the LHD system but also for other helical systems in general. and for tokamaks in the high β operation regime. Although three-dimensional, nonlinear behaviors of an MHD plasma have been extensively investigated for tokamak

1

plasmas (see Mizuguchi et al. [4] for example), little is known about helical plasmas.

Here we concentrate on an MHD plasma to study pressure-driven instabilities in helical systems. This kind of instability is often investigated through linear stability analysis and/or numerical simulations of reduced MHD equations. One of the most successful approaches of stability analysis is the stellarator expansion method which was introduced by Greene and Johnson [5], as well as the averaging method. There are enormous number of works which employ these methods to analyze MHD linear stability of helical plasmas. Refer to a review by Ichiguchi [6] and references therein on these stability analysis.

While linear stability analysis by means of the stellarator expansion method is essentially two-dimensional, there are three-dimensional analysis, too. A series of works by N. Nakajima and his collaborator [7–9] was dedicated to investigate three-dimensional linear ballooning stability. Furthermore, recent numerical codes such as CAS3D [10] and TERPSICHORE [11] are used to investigate linear stability of three-dimensional heliotron equilibria. For example, the CAS3D code was used in Chen et al. [9] for their global mode analysis.

We have to note that development of the stability codes such as CAS3D and TERPSICHORE enabled analysis of three-dimensional instability with low-n modes, where n denotes the toroidal Fourier mode number. Before the development of these codes, it was difficult to analyze low-n sta-

bility of helical systems because of the complexity of their geometry. Most of previous researches on linear analysis have been dedicated to ideal MHD instabilities and properties of a resistive MHD instabilities remain unclarified. On the other hand, some experimental results suggest that plasma behaviors are often dominated by resistive instabilities for low-n modes. For example, Sakakibara et al. [12] have reported that growth of resistive interchange mode were important as much as ideal interchange mode in their Compact Helical System (CHS) experiment.

Nonlinear investigations of helical systems have been conducted by making use of reduced MHD equations, which was first derived by Strauss [13]. There are several works by using reduced MHD equations [14–16], which have succeeded to treat low-n modes concerning internal disruption phenomena. However, fully three-dimensional structures had to be out of scopes of these researches because, from derivation, their reduced MHD systems could express effects of three dimensional helical magnetic structure only in an averaged manner. Thus behaviors of ideal or resistive ballooning modes that strongly depend on local magnetic curvature effects are not understood yet.

In order to investigate complex nonlinear behaviors of an MHD plasma in a three-dimensional structure, we have to execute fully three-dimensional MHD simulations without employing specific approximations for the structure. For this purpose, we

2

have developed a new simulation code which solves a full set of MHD equations in a fully three-dimensional toroidal geometry. This simulation code is a natural extension of the HINT code [17], which obtains a fully three-dimensional equilibrium state without imposing the nested flux assumption. This nonlinear simulation code was originally developed by Hayashi and applied for H1-Heliac simulation under the stellarator symmetry. [18] Then it has been improved to include effects of the shear viscosity and to treat full-torus system. We aim to understand nonlinear behaviors of an MHD plasma in a helical system by making use of the new code. The main target of our investigation is to study evolution and saturation of pressure-driven instabilities which grow in currentless equilibria of helical plasmas and to clarify physical mechanism of relaxation to a possible new equilibrium state. We emphasize that nonlinear investigation on helical MHD plasma including fully three-dimensional structures has seldom been attempted. There are not so much accumulation of knowledge on nonlinear behaviors of helical plasmas. Although our code can treat low-n (fully toroidal) modes by solving entire toroidal system, such a full-torus simulation is expensive as for the computation time. As a first step in the attempt of executing simulations in three-dimensional geometry, we impose the stellarator symmetry in this paper. We assume that some basic nature in nonlinear behavior of pressure-driven instabilities can be observed even in this restricted situation. Actually, as is

shown in Section 3, an indication of a relaxation phenomenon caused by nonlinear evolution of unstable modes is found.

This paper is organized as follows. Section 2 is for outlines of our simulations. Basic equations, boundary conditions, discretization scheme are described there. It is also described how to give an initial condition. Section 3 is for results of nonlinear simulations. Some observation in linear and nonlinear regimes are described there. Concluding remarks are seen in Section 4.

II. OUTLINE OF SIMULATION SCHEMES

A. MHD equations and boundary conditions

We solve time evolution of a full set of nonlinear, non-ideal (dissipative) MHD equations

$$\frac{\partial \rho}{\partial t} = -\frac{\partial}{\partial x_i}\left(\rho V_i\right), \tag{1}$$

$$\frac{\partial\left(\rho V_i\right)}{\partial t} = -\frac{\partial}{\partial x_j}\left(\rho V_i V_j\right) - \frac{\partial p}{\partial x_i} + \epsilon_{ijk} J_j B_k$$
$$+ \mu\left[\frac{\partial^2 V_i}{\partial x_j \partial x_j} + \frac{1}{3}\frac{\partial}{\partial x_i}\left(\frac{\partial V_j}{\partial x_j}\right)\right], \tag{2}$$

$$\frac{\partial p}{\partial t} = -V_j\frac{\partial p}{\partial x_j} - \gamma p\frac{\partial V_j}{\partial x_j} + (\gamma - 1) \times$$
$$\left[\eta J_j J_j + \Phi - \frac{\partial}{\partial x_j}\left(-\kappa\frac{\partial}{\partial x_j}\frac{p}{\rho}\right)\right], \tag{3}$$

$$\frac{\partial B_i}{\partial t} = -\epsilon_{ijk}\frac{\partial}{\partial x_j}\left(-\epsilon_{klm} V_l B_m + \eta J_k\right), \tag{4}$$

$$J_i = \epsilon_{ijk}\frac{\partial B_k}{\partial x_j}, \tag{5}$$

$$\Phi = 2\mu\left[e_{ij}e_{ji} - \frac{1}{3}\left(\frac{\partial V_i}{\partial x_i}\right)\left(\frac{\partial V_j}{\partial x_j}\right)\right], \tag{6}$$

3

$$e_{ij} = \frac{1}{2}\left(\frac{\partial V_i}{\partial x_j} + \frac{\partial V_j}{\partial x_i}\right). \tag{7}$$

The symbols V_i, B_i, J_i and e_{ij} are i-th components of the velocity vector, magnetic field vector, current vector and (i, j) component of the rate-of-strain tensor in the Cartesian coordinate, respectively. The symbols ρ and p represent the density and pressure, respectively. The symbol ϵ_{ijk} represents Edington's anti-symmetric tensor. We take a sum from 1 to 3 on repeated suffices. The conductivity, resistivity and shear viscosity are represented by κ. η and μ, respectively. Equations (1)-(7) are already non-dimensionalyzed by using the characteristic toroidal magnetic field B_0. the toroidal Alfvén velocity $V_a = B_0/\sqrt{\mu_0\rho_0}$ defined by using B_0, the permeability μ_0 and characteristic density ρ_0, and the characteristic length L_0. The geometry is set to simulate the LHD configuration.

Note that dissipative coefficients κ. η and μ are assumed to be constant and isotropic in our simulations. Although non-constant or non-isotropic dissipation models such as the Spitzer resistivity and a conductivity parallel to the magnetic field are often adopted in fusion plasma simulations, we restrict ourselves to the case of constant and isotropic dissipation coefficients in this article because few knowledge are accumulated on numerical behavior of a fully nonlinear MHD plasma in a helical system and we should start from the simplest model. Since the quantities are already non-dimensionalyzed and kept isotropic constants, we may replace the re-

sistivity η by the magnetic Reynolds number (or S-number $S = 1/\eta$).

The MHD equations (1)-(7) are now described in the helical-toroidal coordinate system (u^{1*}, u^2, u^3) which has been adopted in the HINT code. [17] The toroidal-helical coordinate system (u^{1*}, u^2, u^3) used here is described as

$$u^{1*} = u^1 + \delta = r\cos(\theta - h\phi), \tag{8}$$
$$u^2 = r\sin(\theta - h\phi), \tag{9}$$
$$u^3 = -\phi, \tag{10}$$

by the minor radius of the torus r, distance from the origin of the coordinate system δ. the poloidal angle θ and the toroidal angle ϕ. See Fig.1 in Harafuji et al. [17] on the coordinate system. Since we aim to study an MHD plasma in the LHD geometry, we set $\delta = 0$ and a set of values $M = 10$ and $h = M/2$ is adopted throughout this article. The MHD equations in this coordinate system are described in the Appendix A. We impose the stellarator symmetry to this system. The stellarator symmetry consists of $M = 10$ periodic boundary condition on one-pitch period and a sort of symmetric condition on the magnetic field at $\phi = 0$ and at the mid of one-pitch period $\phi = \pi/M$. Boundary conditions on the density, pressure and velocity fields are determined so that the MHD equations (1)-(7) are invariant when the boundary condition is imposed on the magnetic field. Then, the system size of the simulation in the toroidal direction is reduced to one twentieth, $0 \le \phi \le \pi/M$ in toroidal angle, and toroidal mode number available in our simulation is multiples of

4

10. when the mode number is measured in a full-torus geometry. See the Appendix B for the detail of the toroidal boundary conditions in our coordinate system.

In Fig.1, the computational domain is drawn in a gray, twisted rectangular box. The computational domain covers a half-pitch period in the toroidal (u^3) direction. The plasma is assumed to be surrounded by a perfectly conducting wall. A pair of helically-twisted coils of the LHD device and a typical isosurface of the plasma pressure are drawn for readers' convenience to understand the symmetry. The pressure profile used to draw the isosurface is a result of a nonlinear simulation which will be described in the next section. It is seen that the pressure is twisted ten times in the toroidal direction.

Equations (1)-(7) are discretized uniformly in the helical toroidal coordinate system (u^{1*}, u^2, u^3) and the spatial differences are evaluated by the fourth-order central-finite-difference scheme. The resultant discrete equations are marched by the Runge-Kutta-Gill method, which has the fourth-order accuracy in time. Number of the grid points in u^1, u^2, u^3 directions are represented as N_1, N_2 and N_3, respectively. Here N_3 is a grid number for the half period in the toroidal direction. Although we have conducted simulations with $N_1 = N_2 = 49, N_3 = 16$ and $N_1 = N_2 = 97, N_3 = 32$, only latter cases will be shown here.

When we discretized the nonlinear equations to solve numerically, there emerge numerical errors inevitably, which are often called aliasing errors. (See a text by Roache [19], for example.) Removal of aliasing errors is simple and easy when we impose periodic boundary conditions on the system because we only have to operate a low-pass filter to the variables, as is often adopted by well-known spectral methods. [20] The cut-off wavenumber of a low-pass filter must be decided by investigating the nonlinearity of the equations to be solved. However, it is not the case in this article because boundary conditions in u^{1*} and u^2 directions are not periodic. In stead of having a clear-cut de-aliasing by using a low-pass filtering operation, here we make use of a smoothing scheme by taking weighted-average of variables at neighboring grid points. [21] The scheme was adopted by Mizuguchi et al. [4] in their three-dimensional MHD simulations of a spherical tokamak, to show satisfactory results. This scheme contributes not only to removing aliasing errors but to stabilizing the discretized system. Note that relatively large-scale structures have the most unstable nature under the parameters used in this paper. Then the de-aliasing smoothing operation works only to remove small numerical oscillations and does not change physical picture of numerical results.

B. An initial equilibrium obtained by using the HINT code

An initial equilibrium is prepared by using the HINT code [17]. The HINT code is a sort of a relaxation scheme to obtain an ideal MHD equilibrium. In the HINT code,

an initial pressure profile is given by

$$p(\psi) = (1 - \psi^a)^b, \qquad (11)$$

where ψ represents an initial magnetic flux function. Parameters a and b controls the initial profile of the pressure. Here a set of parameters $a = 1$ and $b = 2$ is adopted. The choice of parameters is the same with Ichiguchi et al. [22] who have studied the Mercier stability of the LHD system by using the VMEC code [23]. We study a case where the major radius of the vacuum magnetic axis R_{ax} is located at $R_{ax} = 3.7m$ in the real dimension. This case corresponds to a case where the vacuum axis is slightly inwardly shifted. (The center of the helical coil for LHD is located at $3.9m$ in the major radius.) In this paper, we restrict ourselves to an initial equilibrium whose central beta β_0 is 4%. According to a previous study [22], a part of magnetic surfaces for an equilibrium with $R_{ax} = 3.7m$ and $\beta_0 = 4\%$ are analyzed to be unstable for the Mercier criterion.

In Figs.2(a) and (b), Poincare plots of the magnetic field lines on horizontally- and vertically-elongated poloidal sections at $\phi = 0$ and $\phi = \pi/M$, respectively, are shown. Hereafter, in figures of Poincare plots and contour plots, the right-hand side represents the outer side of the torus both for the horizontally- or vertically-elongated cross-sections. Poincare plots and contour plots in a horizontally- (vertically-) elongated rectangular box represent those on a horizontally- (vertically-) elongated cross-section. We see in Fig.2(a) and (b) that the

Shafranov shift has put the position of the magnetic axis toward outer side of the torus. Consequently, the magnetic axis is observed relatively in the right-hand side in Figs.2(a) and (b). In Fig.2(c), the profile of the rotational transform $\iota/2\pi$ is shown. The abscissa represents the averaged minor radius. In Fig.2(d) a bird's eyes view of the pressure on a horizontally-elongated poloidal section is shown. It is seen that the pressure has a clear bell-shape which is a natural result of the parameter set $a = 1, b = 2$ for the initial pressure profile of the HINT code. In Fig.2(e), a bird's eyes view of the toroidal current on the same poloidal section with Fig.2(d) is shown. It is seen that the Pfirsch-Schlüter current is emerging on the center of the poloidal section keeping the net toroidal current null.

III. NONLINEAR SIMULATION

A. An observation of a resistive ballooning instability

Now we investigate time evolution of the MHD equations (1)-(7). In Fig.3, time evolution of the kinetic energies obtained by typical three simulations is shown. The conductivity κ and shear viscosity μ were set 1×10^{-6} and 2×10^{-3}, respectively, and the resistivity were varied $\eta = 1 \times 10^{-6}$(solid line), 1.78×10^{-6}(dashed line) and 3.16×10^{-6} (dotted line). The conductivity κ is fixed to 1×10^{-6} throughout this article. First we observe some overshoots of the kinetic energy in the very early phase of

6

the time evolution. It is typically observed in simulations when random perturbations which are not proportional to linear eigenfunction are given. After the overshoots. the kinetic energy stays almost constant for a period for about from $t = t_s = 400\tau_A$ (dotted line) to $t = t_s = 700\tau_A$ (solid line). It is considered to be a period when the linear eigenfunction at unstable modes is gradually formed out of tiny random perturbations. At around $t = t_s$, the kinetic energy begins an exponential growth until nonlinearity of MHD equations (1)-(7) cause saturations.

Now we study behaviors of the pressure during the exponential growth observed in Fig.3. Hereafter, so far as we do not note explicitly, we investigate various quantities for the case of $\eta = 3.16 \times 10^{-6}$ and $\mu = 2 \times 10^{-3}$. In Figs.4(a) and (b), contour plots of the pressure on a horizontally- and a vertically-elongated poloidal sections are shown, respectively. Here the time $t = 520\tau_A$ corresponds to relatively early stage of the exponential growth. There are some deformations of the pressure contours in the outer side of the torus. In order to investigate these deformations, contour plots of modulo of the pressure fluctuation on horizontally- and vertically- elongated poloidal sections are shown in Figs.4(c) and (d), respectively. We see that the pressure fluctuation is localized around a circular region where the pressure gradient becomes the steepest. The fluctuation is especially large in the outer side of the torus. Note that the de-stabilization effect of the magnetic curvature becomes strongest on the outer-

side of horizontally-elongated poloidal section for the heliotron type helical configuration. These observations suggest that the exponential growth was caused by a kind of ballooning instability. It is considered that a weak interchange instability has also contributed to the pressure deformation because there are small deformations in the inner side of the torus. (Recall that our initial equilibrium solution is expected to be Mercier-unstable.) As time proceeds, wavy contours of the pressure grows toward edge regions. especially in the outer side of the torus. We observe in Figs.4(e) and (f) that ridges of the pressure contours slightly bend into the inner side of the torus. It looks that these ridges are growing toward the radial direction of a magnetic coordinate. [6] At this stage of the time evolution, the energy growth is not exponential any more and going to saturate by nonlinear effects, though the plasma still seems to be dominated by the most unstable mode. An isosurface of the pressure at $t = 890\tau_A$ is seen in Fig.1. It is clearly seen that ridges of the pressure isosurface have grown strongly toward outer side of the torus while the ridges in the inner side of the torus are very small.

In order to look closely into the origin of the exponential growth and pressure deformation observed above. we have conducted a survey on various resistivities on a range $1 \times 10^{-6} \leq \eta \leq 3.16 \times 10^{-4}$ for two values of the viscosity $\mu = 1 \times 10^{-3}$ and 2×10^{-3}. In all of simulations, the exponential growth of the kinetic energy and wavy contours of the pressure in the outer side of the torus are

7

observed. The exponential growth regions were identified and fitted by an exponential function in order to obtain growth rates of the most unstable mode. In Fig.5, the growth rates are shown as a function of the resistivity. It is seen that the growth rate is almost proportional to $\eta^{1/3}$ both for the case of $\mu = 1 \times 10^{-3}$ and 2×10^{-3}. Previous investigations [15,24] have shown that both resistive interchange and resistive ballooning instability brings growth rates proportional to $\eta^{1/3}$. Because of the pressure deformation observed in Figs.4, these growth are considered to be caused by the resistive ballooning instability. (We have to keep in mind that the linear analysis by Depassier and Cooper [24] is based on a large-aspect-ratio expansion. Since the aspect ratio of the LHD is about 6, we have to be careful to compare our results with their analysis.)

Poloidal mode number of the ballooning instability observed in these simulations is $m = 15$ as far as we identify the mode by counting number of ridges of the pressure contours, local maxima of module of the pressure fluctuation, and number of islands observed in Poincare plots of the magnetic field lines. Since the ballooning mode was first observed at the region $\iota/2\pi \simeq 2/3$, where the pressure gradient become the steepest. the toroidal mode number is considered to be $n = 10$, which is the smallest toroidal number available in our simulations. There observed little dependence of number of these ridges of the pressure contours, or the poloidal mode number of the most

unstable mode, on the resistivity. It may be understood as follows. The toroidal mode numbers available in our simulations are restricted to multiples of 10. The region at which a ballooning mode should emerge first is roughly determined by the steepest pressure gradient. It is the region $\iota/2\pi \simeq 2/3$ in our initial equilibrium. Then the poloidal mode numbers which we expect to emerge are $m = 15$ and multiples of it. Under the value of the shear viscosity we used, poloidal mode numbers much greater than $m = 15$ are suppressed. Consequently we have only $m \simeq 15$ poloidal mode number. Remember that the mode structure was identified through number of ridges of pressure contours or local maxima of the modulo of pressure fluctuation and that ballooning mode is realized by coupled set of poloidal Fourier modes [25]. Thus it is considered that there exist some poloidal numbers around $m \simeq 15$ associated with $\iota/2\pi \simeq 2/3$.

Now we pay attention to the growth rates associated with $\eta \leq 1.78 \times 10^{-6}$ in Fig.5. Some of growth rates in this resistivity region do not obey to the scaling $\eta^{1/3}$. We have to note two comments here. One is that the growth rates with $\mu = 1 \times 10^{-3}$ and $\eta < 1 \times 10^{-6}$ gave almost the same growth rates with the case $\mu = 1 \times 10^{-3}$ and $\eta = 1 \times 10^{-6}$. We consider that a numerical dissipation caused by the finite difference scheme exceeds the physical effect of the resistivity for $\eta \leq 1 \times 10^{-6}$. Then the effective value of the resistivity should be greater than 1×10^{-6} even when η was set 1×10^{-6}, to cause a larger growth rate

8

than the value expected by $\eta^{1/3}$-scaling.

Another one is on a deformation of the pressure for the cases $\mu = 2 \times 10^{-3}$ and $\eta \leq 1.78 \times 10^{-6}$. Their small growth rates lead the plasma to the long exposure under conductive effects and ohmic heating during the period of the formation of eigenfunction. as was observed in Fig.3. We deduce that exposure by the nonideal dissipation effects for sufficiently long period caused change of the equilibrium and brought departure of the growth rate from the scaling $\eta^{1/3}$.

B. Nonlinear deformation of the pressure profile

Next we see deformation of the pressure after the nonlinear saturation of the kinetic energy observed in Fig.3. Again we concentrate on the case of $\eta = 3.16 \times 10^{-6}$ and $\mu = 2 \times 10^{-3}$. Contour plots of the pressure at $t = 1430\tau_A$ on horizontally- and vertically-elongated poloidal sections are shown in Figs.6(a) and (b). respectively. Bends of ridges of the pressure contours toward the inner sides of the torus are more clearly seen in Figs.6(a) and (b) than in Figs.4(e) and (f). Thus the bends of the pressure ridges. which can be seen as if they are going toward the radial direction of a magnetic coordinate. are considered to be a result of nonlinear phenomenon. In the inner side of the torus in Figs.6, we observe there are some regions where the pressure contours are relatively sparse. The pressure gradient is small there. On the other hand. the pressure gradient is very large

in the outer side of the torus. In Figs.6(c) and (d). contour plots of the pressure at $t = 1700\tau_A$ on horizontally- and vertically-elongated poloidal sections are shown. The pressure contours are less concentrated than those in Figs.6(a) and (b), to show that the plasma profile is changing toward a new relaxed state.

The Poincare plots of the magnetic field lines associated with cross-sections in Figs.6 are shown in Figs.7. Although the magnetic field lines are stochastic in Figs.7(a) and (b). there are clear magnetic surfaces at the center region of the plasma. The plasma is still well confined inside the nested magnetic surfaces. In Figs.7(a) and (b), there are also many remains of magnetic surfaces and/or islands which prevent the magnetic field lines from becoming fully stochastic. These remains of magnetic surfaces and islands seem becoming clearer in Figs.7(c) and (d) compared with (a) and (b) respectively. suggesting that the plasma confinement is going to be recovered. As far as the central part of the plasma is concerned, we find appearance of new magnetic islands in Figs.7(c) and (d). We do not find any magnetic islands there in Figs.7(a) and (b). It means that a new unstable mode is growing around this region. We will come to this point in the last section.

We see a one-dimensional plot of the pressure at $t = 1700\tau_A$ in Figs.8. The abscissa is a vertical axis u^2 which go across the point with the maximum value of the pressure on a vertically-elongated poloidal section. Readers may be able to understand

9

u^2 as a minor radius r in this case because the magnetic axis is located on $u^2 = 0$. We observe that the pressure profile is quite polygonal. The core part $u^2 \simeq 0$, at which a plasma is confined by the nested magnetic surfaces, is surrounded by a very steep gradient of the pressure. It is considered that this steep gradient of the pressure becomes a source of a new pressure-driven instability there. At the low-pressure region, there observed two stages of flattened pressure around $|u_2| \simeq 0.3$ and $|u_2| \simeq 0.5$. As is shown in the next figures, this structure is brought by a ballooning instability. At the edge region $|u_2| > 0.5$, we observe the pressure profile looks something like the pedestal structure observed in LHD experiments. [3]

A bird's eyes views of the pressure at $t = 1700\tau_A$ are shown in Figs.9. In Fig.9(a), a bird's eyes view of the pressure on horizontally-elongated poloidal section is shown. The inner side of the torus is in the left-hand side of this view. It is clearly observed that ridges of the pressures are twined around the core part of a confined plasma. Furthermore, there are some locally-peaked pressure profile in the inner-side of the torus. Much more number of small peaks of the pressure are observed in Fig.9(b), a bird's eyes view of the pressure on vertically-elongated poloidal section. It is a view from the inner side of the torus. Trains of small peaks consists of a couple of layers in the radial direction. These small peaks of pressure are associated with magnetic islands observed in Figs.7.

A comparison of pressure profiles in Figs.6(c) and (d), Fig.8 and Figs.9 reveals that the flattened pressure profile observed in Fig.8 have been formed along the pressure ridges which we have observed in Figs.6. In fact, by observing contours in Figs.6, we find that there are regions with sparse contours along pressure ridges both on horizontally- and vertically-elongated poloidal sections. Note that the two pressure ridges observed in Fig.9(b) forms a pedestal-like pressure silhouette at the edge regions, associated with one-dimensional plot in Fig.8. Thus we may be able to attribute the origin of this pedestal-like structures to the resistive ballooning instability and its nonlinear evolution which has formed these pressure ridges. Since the pressure ridges are growing along the radial direction of the magnetic coordinate, some analysis on this coordinate system may contribute to clarify the mechanism of the flattened pressure formation.

IV. CONCLUDING REMARKS

We have reported results on nonlinear simulation of an MHD plasma that is executed in the full three-dimensional geometry of the LHD system. In this paper, we focused on plasma behavior in the medium poloidal mode number range by imposing the sterallator symmetry boundary conditions in the toroidal direction. Growth and saturation of the resistive ballooning modes were observed. We found that the growth rate of the kinetic energy in the linear growth period were proportional to $\eta^{1/3}$.

10

In nonlinear stages of our simulations. we observed that magnetic surfaces are going to be recovered in the edge region of the plasma while a new instability is coming up in the center region. It was observed in Figs.7 that magnetic surfaces at the region where the ballooning instability had emerged first were recovered while a new ballooning instability was going to occur in the inner side of poloidal sections. A scenario of nonlinear relaxation which is consistent with above observation is described as follows.

1. A ballooning instability is first observed in a region with the steepest pressure gradient. It causes convective transport of the plasma heat energy from the inner region to the edge region through the region under the instability grows.

2. While the first instability initially excited is stabilized by a nonlinear effect (reedistribution of the pressure) and viscosity, it prepares next instability by making the pressure gradient in the inner side of the poloidal section steeper. This process continues till the steep pressure region in the core region disappears.

3. When the final instability in the central part of the poloidal section is stabilized, the overall profile of the plasma pressure becomes broader, and it appears that the system relaxes toward a new equilibrated state.

In order to consider whether this rough scenario seems to occur or not. contour plots of the pressure and Poincare plots of the magnetic field lines on horizontally- and vertically-elongated poloidal sections at $t = 4000\tau_A$, far beyond the last time in Fig.3 are shown in Figs.10. We observe that the pressure profile is well-shaped and the magnetic surfaces are recovered clearly in Figs.10. Although a computation with finer resolutions might be required to confirm such a long time scale behavior. we consider Figs.10 suggest a possible recovery of the equilibrium state as a result of a series of nonlinear relaxation processes according to a scenario described above.

In nonlinear stages of our simulations. we observed structures which look similar to pedestal structures observed in LHD experiments [3]. Although it may be in controversy on what the origin of the pedestal is, it is worth keeping in mind that similar structures can be observed in MHD simulations. It is also noteworthy that this structure is observed along the pressure ridges. which have been formed as a result of nonlinear evolution of ballooning instability.

ACKNOWLEDGMENT

11

REFERENCES

[1] O. Motojima et al., Phys. Plasmas 6, 1843 (1999).

[2] H. Yamada et al., Phys. Rev. Lett. 84, 1216 (2000).

[3] N. Ohyabu et al., Phys. Rev. Lett. 84, 103 (2000).

[4] N. Mizuguchi et al., Phys. Plasmas 7, 940 (2000).

[5] J. M. Greene and J. L. Johnson, Phys. Fluids 4, 875 (1961).

[6] K. Ichiguchi. Recent Res. Devel. Plasmas 1, 101 (2000)

[7] N. Nakajima, Phys. Plasmas 3, 4545 (1996).

[8] N. Nakajima, Phys. Plasmas 3, 4546 (1996).

[9] J. Chen et al., Phys. Plasmas 6, 1562 (1999).

[10] C. Schwab, Phys. Fluids B5, 3195 (1993)

[11] D. V. Anderson et al., in Proc. Joint Varenna-Lausanne International Workshop on Theory and Fusion Plasmas (Bologna, 1988) 93.

[12] S. Sakakibara et al., J. Phys. Soc. Japan 63, 4406 (1994).

[13] H. R. Strauss, Plasma Phys. 22 733 (1980).

[14] M. Wakatani, H. Shirai and M. Yamagiwa , Nucl. Fusion 24, 1407 (1984)

[15] K. Ichiguchi, Y. Nakamura and M. Wakatani , Nucl. Fusion 31, 2073 (1991)

[16] B. A. Carreras, V. E. Lynch, H. Zushi, K. Ichiguchi, and M. Wakatani , Phys. Plasmas 5, 3700 (1998)

[17] H. Harafuji, T. Hayashi and T. Sato, J. Comp. Phys. 81, 169 (1989)

[18] T. Hayashi, Proc. 3rd Australia-Japan Workshop on Plasma Theory and Computation (Robertson, 1995) Australia National Univ. Cambera 26 (1995).

[19] P. J. Roache, Computational Fluid Dynamics, Hermosa Publishers Inc., (1974)

[20] C. Canuto et al., Spectral Methods in Fluid Dynamics, Springer-Verlag, N.Y. (1987)

[21] Birdsall and Langdon, Plasma Physics via Computer Simulation, McGraw-Hill, N.Y.(1985)

[22] K. Ichiguchi et al., Nucl. Fusion 33, 481 (1993)

[23] S. P. Hirshman et al., Comp. Phys. Comm. 43, 143 (1986)

[24] M. C. Depassier and W.A. Cooper, Phys. Fluids 29, 1948 (1986)

[25] R.D. Hazeltine and J.D. Meiss, Phys. Reports 121, 1 (1985).

The MHD equations (1)-(7) are described in the helical-toroidal coordinate system (8)-(10) as follows.

$$\frac{\partial \rho}{\partial t} = \frac{1}{\sqrt{g}} \frac{\partial \left(\sqrt{g}\rho v^i\right)}{\partial u^i}, \qquad (A1)$$

$$\frac{\partial \rho v^i}{\partial t} = -g^{ih}\left[\frac{\partial T_h^k}{\partial u^k} + \left\{\begin{matrix} k \\ lk \end{matrix}\right\} T_h^l \right.$$
$$\left. - \left\{\begin{matrix} l \\ hk \end{matrix}\right\} T_l^k + \epsilon_{ikh}j^k b^h \right]$$
$$+ \mu\left[-\frac{1}{\sqrt{g}}\epsilon_{ikh}\frac{\partial}{\partial u^k}\left(g_{hl}\frac{1}{\sqrt{g}}\epsilon_{lmn}\frac{\partial v^n}{\partial u^m}\right)\right.$$
$$\left. + \frac{4}{3}\frac{\partial}{\partial u^i}\left\{\frac{1}{\sqrt{g}}\frac{\partial\left(\sqrt{g}v^i\right)}{\partial u^i}\right\}\right] \qquad (A2)$$

$$T_i^k = \rho v^i v_k + p\delta_{ik}, \qquad (A3)$$

$$\frac{\partial p}{\partial t} = -v^i\frac{\partial p}{\partial u^i} - \gamma p\frac{1}{\sqrt{g}}\frac{\partial\left(\sqrt{g}v^i\right)}{\partial u^i}$$
$$+ (\gamma - 1) + \left[\eta j^i j_i + \Phi\right.$$
$$\left. + \kappa\frac{1}{\sqrt{g}}\frac{\partial}{\partial u^i}\left(\sqrt{g}\frac{\partial}{\partial u_j}\frac{p}{\rho}\right)\right], \qquad (A4)$$

$$\frac{\partial b^i}{\partial t} = -e_{ikh}\frac{1}{\sqrt{g}} \times$$
$$\frac{\partial}{\partial u^k}\left(-\sqrt{g}\epsilon_{hlm}v^l b^m + \eta j^h\right), \qquad (A5)$$

$$j_i = \frac{1}{\sqrt{g}}\epsilon_{ikl}\frac{\partial b_l}{\partial u^k}, \qquad (A6)$$

$$\Phi = 2\mu\left[s_{ij}s_{ji} - \frac{1}{3}\times\right.$$
$$\left. \left(\frac{1}{\sqrt{g}}\frac{\partial\left(\sqrt{g}\rho v^i\right)}{\partial u^i}\right)^2\right], \qquad (A7)$$

$$s_{ij} = M_{ik}e_{kj}, \qquad (A8)$$

$$\overline{\mathbf{M}} = \frac{\partial\left(u^1, u^2, u^3\right)}{\partial\left(x_1, x_2, x_3\right)}. \qquad (A9)$$

Here g_{ij}, g^{ij} and g are (i,j)-components of covariant and contravariant components of metric tensor and square of the Jacobian, respectively. The symbol

$$\left\{\begin{matrix} h \\ ij \end{matrix}\right\} = \left\{\begin{matrix} h \\ ji \end{matrix}\right\} = \frac{1}{2}g^{hp}\left(\frac{\partial g_{ip}}{\partial u^j} + \frac{\partial g_{jp}}{\partial u^i} + \frac{\partial g_{ij}}{\partial u^p}\right) \qquad (A10)$$

is the Christoffel symbol. Symbols v^i, b^i and j^i represent i-th contravariant components of the velocity, magnetic field and current vectors, respectively, while variable with subscripts represent contravariant components which can be obtained by using the metric tensors g_{ij} or g^{ij}. The bold face symbol $\overline{\mathbf{M}}$ represents a 3×3 Jacobian tensor and its (i,j) components are represented by the symbol M_{ij}. In eq.(A2), we have used the vector identity

$$\nabla^2 \mathbf{v} = \nabla\left(\nabla\cdot\mathbf{v}\right) - \nabla\times\left(\nabla\times\mathbf{v}\right) \qquad (A11)$$

for ease of a mathematical expression of the the Laplacian of a vector $\mathbf{v}$. In eq.(A4), we have also used a fact that the dissipative coefficients are isotropic constant.

APPENDIX B

As was described in Section 2, the stellarator symmetry is imposed in the toroidal direction of this system. The boundary conditions associated with the stellarator symmetry on the contravariant components of the magnetic field vector may be described as

$$b^1(u^1, u^2, \Delta u^3) = -b^1(u^1, -u^2, -\Delta u^3), \qquad (B1)$$
$$b^2(u^1, u^2, \Delta u^3) = b^2(u^1, -u^2, -\Delta u^3), \qquad (B2)$$
$$b^3(u^1, u^2, \Delta u^3) = b^3(u^1, -u^2, -\Delta u^3), \qquad (B3)$$

on the poloidal section $\wp = 0$ (vertically-elongated poloidal section), and

$$b^1(u^1, u^2, \pi/M - \Delta u^3)$$
$$= b^1(-u^1, u^2, \pi/M + \Delta u^3), \quad \text{(B4)}$$
$$b^2(u^1, u^2, \pi/M - \Delta u^3)$$
$$= -b^2(-u^1, u^2, \pi/M + \Delta u^3), \quad \text{(B5)}$$
$$b^3(u^1, u^2, \pi/M - \Delta u^3)$$
$$= b^3(-u^1, u^2, \pi/M + \Delta u^3), \quad \text{(B6)}$$

on the section $\wp = \pi/M$ (horizontally-elongated poloidal section), where Δu^3 is the grid interval along the u^3 direction. Boundary conditions on the density, pressure and velocity fields are determined so that the MHD equations (1)-(7) are invariant when the boundary condition is imposed on the magnetic field, and described as

$$\rho(u^1, u^2, \Delta u^3) = \rho(u^1, -u^2, -\Delta u^3), \quad \text{(B7)}$$
$$p(u^1, u^2, \Delta u^3) = p(u^1, -u^2, -\Delta u^3), \quad \text{(B8)}$$
$$v^1(u^1, u^2, \Delta u^3) = v^1(u^1, -u^2, -\Delta u^3), \quad \text{(B9)}$$
$$v^2(u^1, u^2, \Delta u^3) = -v^2(u^1, -u^2, -\Delta u^3). \quad \text{(B10)}$$
$$v^3(u^1, u^2, \Delta u^3) = -v^3(u^1, -u^2, -\Delta u^3), \quad \text{(B11)}$$

on the poloidal section $\phi = 0$, and

$$\rho(u^1, u^2, \pi/M - \Delta u^3)$$
$$= \rho(-u^1, u^2, \pi/M + \Delta u^3), \quad \text{(B12)}$$
$$p(u^1, u^2, \pi/M - \Delta u^3)$$
$$= p(-u^1, u^2, \pi/M + \Delta u^3), \quad \text{(B13)}$$
$$v^1(u^1, u^2, \pi/M - \Delta u^3)$$
$$= -v^1(-u^1, u^2, \pi/M + \Delta u^3), \quad \text{(B14)}$$
$$v^2(u^1, u^2, \pi/M - \Delta u^3)$$
$$= v^2(-u^1, u^2, \pi/M + \Delta u^3), \quad \text{(B15)}$$
$$v^3(u^1, u^2, \pi/M - \Delta u^3)$$
$$= -v^3(-u^1, u^2, \pi/M + \Delta u^3), \quad \text{(B16)}$$

at $\wp = \pi/M$.

Figure captions

Fig.1 Computational domain, LHD coils and an isosurface of the pressure. A gray, twisted rectangular box represents the computational domain in which an MHD plasma is simulated in our simulations. The box has half-pitch period in the toroidal direction. LHD coils and an isosurface of the pressure obtained in our simulation are drawn in fully toroidal geometry.

Fig.2 Profiles of an initial equilibrium state obtained by the HINT code. Poincare plots of magnetic lines on a horizontally and vertically elongated poloidal sections, $\phi = 0$ and π/M are shown in (a) and (b), respectively. Magnetic axis is in the right-hand side of the center of the rectangular poloidal section in (a) and (b), because of the Shafranov shift. The rotational transform $\iota/2\pi$ in (c) shows a magnetic well, which is typical to the traditional stellarator such as LHD. Birds' eyes view of the pressure and toroidal current on a poloidal section are shown in (d) and (e), respectively.

Fig.3 Time evolution of the kinetic energy. Solid, dashed and dotted lines represent runs with the resistivity $\eta = 1 \times 10^{-6}, 1.78 \times 10^{-6}, 3.16 \times 10^{-6}$, respectively. The conductivity and shear viscosity are 1×10^{-6} and 2×10^{-3}, respectively.

15

Fig.4 Pressure contours on horizontally-
and vertically-elongated poloidal sec-
tions at $\tau_A = 520$ are shown in (a) and
(b), respectively, for the case of $\eta =$
3.16×10^{-6} and $\mu = 2 \times 10^{-3}$. Con-
tours of pressure fluctuations associ-
ated with (a) and (b) are shown in (c)
and (d), respectively. Pressure con-
tours on horizontally- and vertically-
elongated poloidal sections at $\tau_A =$
890 are shown in (e) and (f), respec-
tively.

Fig.5 Growth rates obtained in the regime
of exponential growth. The black tri-
angles and circles are associated with
the viscosity $\mu = 1 \times 10^{-3}$ and 2×10^{-3},
respectively.

Fig.6 Pressure contours on horizontally-
and vertically-elongated poloidal sec-
tions at $t = 1430\tau_A$ are shown in
(a) and (b), respectively, and those at
$t = 1700\tau_A$ are shown in (c) and (d),
respectively.

Fig.7 Poincare plots of the magnetic field
lines on the poloidal sections associat-
ed with Fig.6.

Fig.8 A deformation of the pressure pro-
file caused by a nonlinear saturation
of the resistive ballooning instability.

Fig.9 Birds' eyes view of the pressure on
a (a)horizontally- and (b)vertically- e-
longated poloidal sections.

Fig.10 Contours of the pressure and
Poincare plots of the magnetic field

lines on the poloidal sections associ-
ated with Fig.6.

16

FIGURES
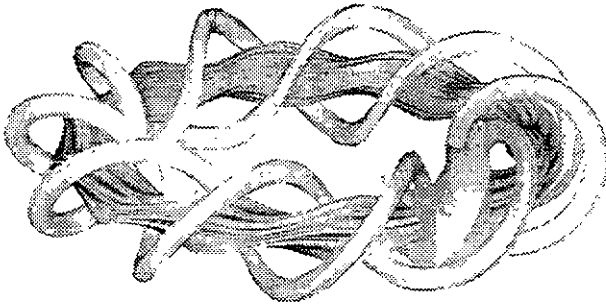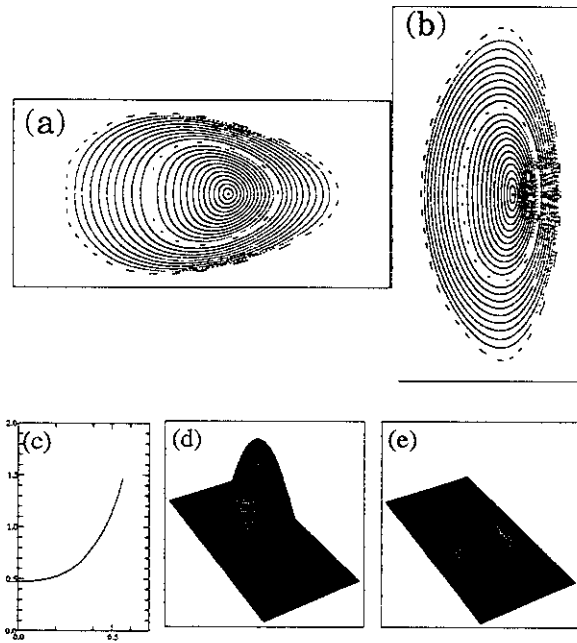
FIG. 1.

FIG. 2. (a)-(e)
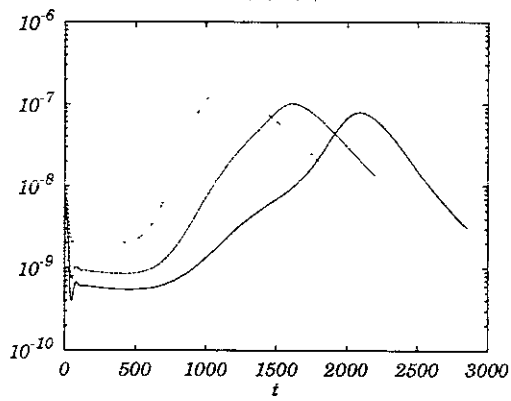
FIG. 3.

FIG. 4. (a)-(f)

FIG. 5.

FIG. 7. (a)-(d)

FIG. 6. (a)-(d)

FIG. 8.

(a)

(b)
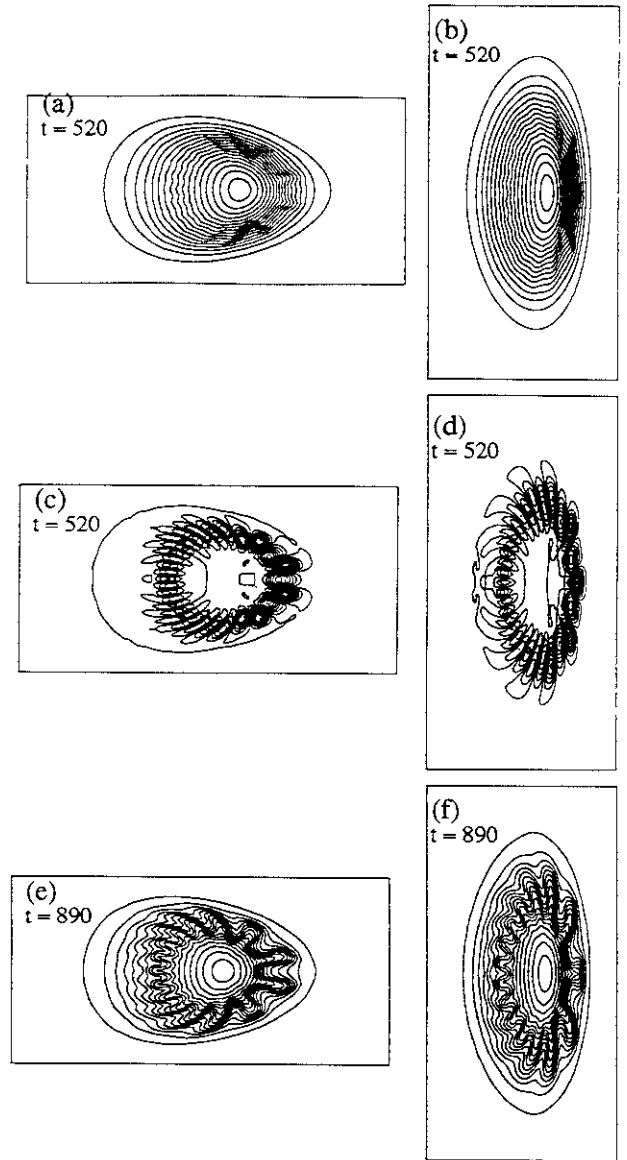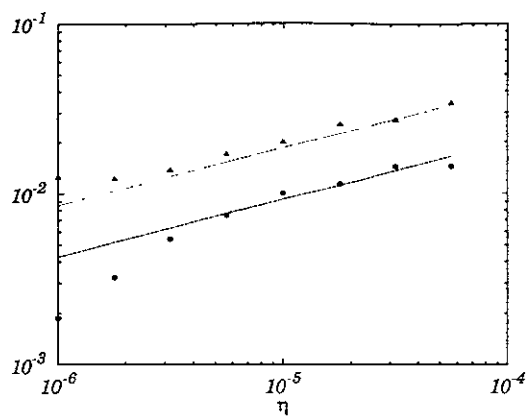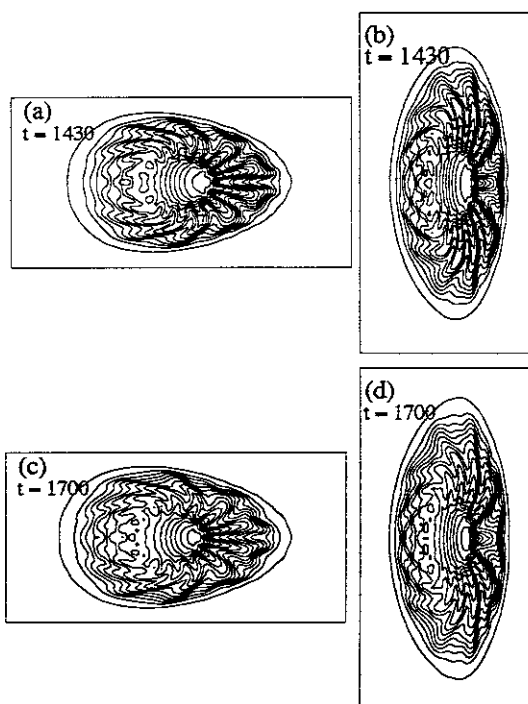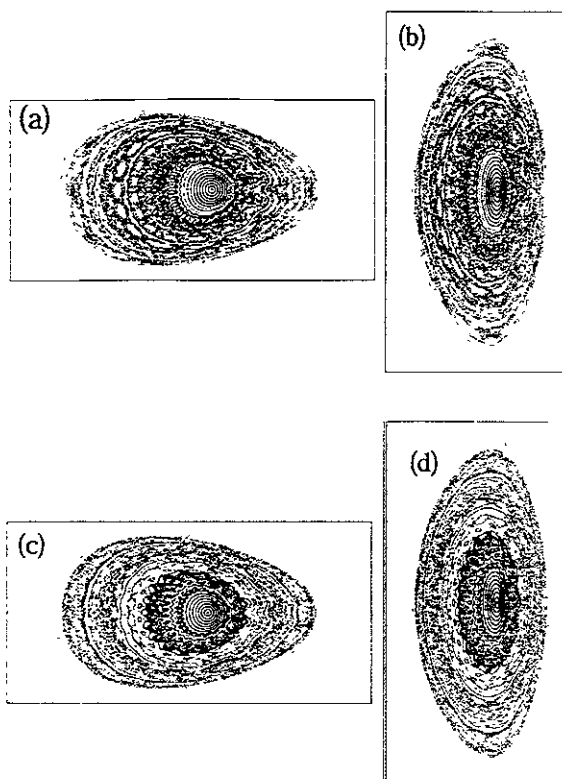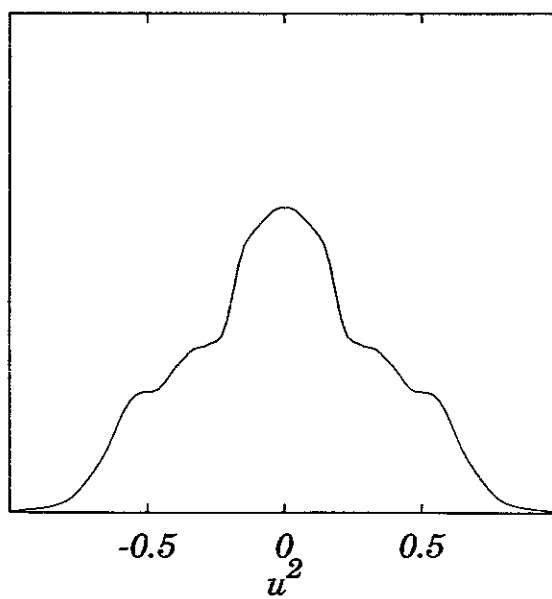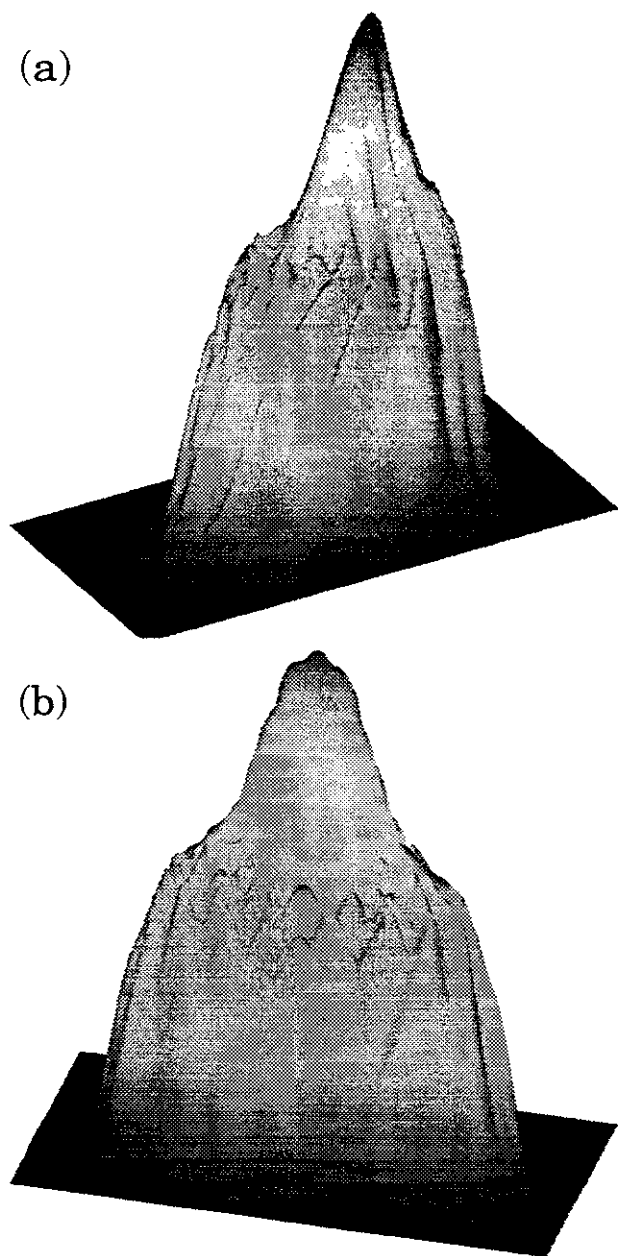
FIG. 9. (a),(b)
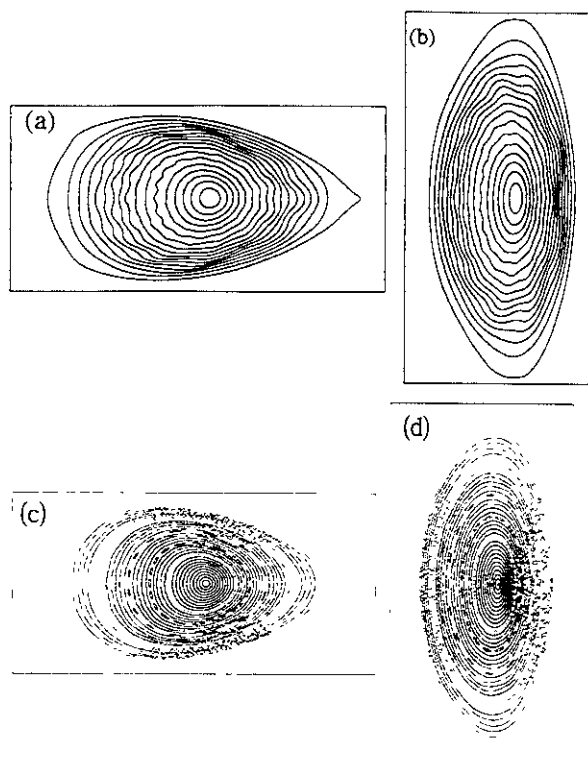
FIG. 10. (a)-(d)

Recent Issues of NIFS Series